Check for updates

Pore development in viscoelastic foods during drying†

Ruud van der Sman, ◑ ⋆[ab] Michele Curatolo[c] and Luciano Teresi[c]

In this paper, we present a numerical model that can describe the pore formation/cavitation in viscoelastic food materials during drying. The food material has been idealized as a spherical object, with a core/shell structure and a central gas-filled cavity. The shell represents a skin as present in fruits/vegetables, having a higher elastic modulus than the tissue, which we approximate as a hydrogel. The gas-filled pore is in equilibrium with the core hydrogel material, and it represents pores in food tissues as present in intercellular junctions. The presence of a rigid skin is a known prerequisite for cavitation (inflation of the pore) during drying. For modeling, we follow the framework of Suo and coworkers, describing the inhomogeneous large deformation of soft materials like hydrogels – where stresses couple back to moisture transport. In this paper, we have extended such models with energy transport and viscoelasticity, as foods are viscoelastic materials, which are commonly heated during their drying. To approach the realistic properties of food materials we have made viscoelastic relaxation times a function of T_g/T, the ratio of (moisture dependent) glass transition temperature and actual product temperature. We clearly show that pore inflation only occurs if the skin gets into a glassy state, as has been observed during the (spray) drying of droplets of soft materials like foods.

1 Introduction

During drying often pore development occurs, such as during drying of polymeric food materials[1–4] or conventional air drying of vegetables.[5–8] A requirement for this pore formation is the development of an elastic skin,[4] which can happen either *via* gelling or *via* entering the glassy state.[9] For vegetables, the skin formation is called case-hardening, where the biopolymer network of the cell wall material densifies with an increase in the elastic modulus. The case-hardened skin can even get into the glassy state.[10]

Further shrinkage of the food material leads to build up of elastic stresses in the skin. The gradients in the stress lead to the development of underpressure in the core of the material. If pre-existing pores exist they will expand, or otherwise, pores can nucleate if the underpressure reaches a critical value, which grows by an increase of the underpressure. This mechanism of pore formation during drying is valid using numerical models, representing vegetables as a hydrogel covered with an elastic skin and a central pore (cavity).[11,12]

In this model, we have assumed that the vegetable is a purely elastic hydrogel, with the stress and chemical potential of water following from a free energy functional, which can be viewed as a generalization of the Flory–Rehner theory. Vegetables as a hydrogel is a reasonable approximation, as the cell wall material can be regarded as a biopolymer network. Consequently, Flory–Rehner theory has been used to describe the hydration (water holding capacity) of vegetables.[13] However, fruits and vegetables are also viscoelastic materials.[14,15]

Flory–Rehner theory is limited in modelling the drying, as it assumes isotropic and uniform deformation of the material. This limitation was overcome in the theory developed by Suo and coworkers, which is capable of handling anisotropic and inhomogeneous deformation[16,17] – which has been applied in our earlier models.[11,12] There we solved the mass balance for moisture, coupled to the steady state momentum equation ($\nabla \cdot \sigma = 0$). Importantly, Suo and coworkers consider hydrogels as a single phase, governed by a single thermodynamic potential (*i.e.* a single stress tensor, chemical potential, and pressure), in line with Flory–Rehner theory.

We must note that in other fields similar systems have been treated as multiphase systems,[18–21] where the polymer matrix and water are considered separate thermodynamic phases, each with its pressure – building on the work in poroelasticity. In our definition,[22] one can speak of a multiphase system if the phases are immiscible and are bounded by interfaces. Porous media such as rock formations are an example of a multiphase

[a] *Wageningen-Food & Biobased Research, Wageningen University & Research, The Netherlands. E-mail: ruud.vandersman@wur.nl*

[b] *Food Process Engineering, Wageningen University & Research, The Netherlands*

[c] *Universita degli Studi Roma Tre, Italy. E-mail: michele.curatolo@uniroma3.it, teresi@uniroma3.it*

† Electronic supplementary information (ESI) available. See DOI: https://doi.org/10.1039/d4sm00201f

system, where inert, non-hygroscopic particles are dispersed in a fluid, which can be a mixture of water and gas. Originally, the poroelastic theory was developed by Biot for porous media like soil and rock, and has probably contributed to the incorrect view of hydrogels as a multiphase system.

In this paper, we like to extend our previous model towards viscoelastic food materials. Pore formation occurs in several food applications: (a) spray drying of maltodextrin, where pore formation occurs *via* cavitation, if a gel-like skin is formed,[4] (b) pore formation in pre-dried vegetable snacks *via* an instant pressure drop (DIC),[23] and (c) pore formation during hot air drying of vegetables, as induced by case hardening,[10] (d) pore formation during drying of seeds, and (e) puffing of bubbles in heated starchy snacks.[10,24] The interplay between the pressure drop and time development of porosity also plays a role in the DIC treatment of non-predried mushrooms,[25] but this system is different from the above, as the mushroom is a porous system with high interconnectivity, while the other systems have closed pores. It is shown in multiple publications[14,15,26–29] that these food materials must be treated as viscoelastic materials, which dissipated elastic stresses at a time scale shorter or comparable to the time scales of drying.

These applications in food drying possess similarities to other problems in soft matter, such as cavitation in soft matter induced by drying.[30–36] These studies are often inspired by the natural phenomenon like the spore dispersal by ferns, which use the conversion of the collapse of a cavity to kinetic energy for projecting spores[37] or emboli formation in vascular tissues in trees.[38]

We intend to develop eventually a 3D finite element model in COMSOL, such that the model can also predict other mechanical instabilities like wrinkling and creasing. In previous models, we have assumed isothermal and pure elastic food materials.[11,12] In this paper, we extend our earlier 1D model to viscoelastic food materials, which are also subject to heating. However, we retain the above simple spherical geometry. The extension of the model to 3D is for the future study.

The viscoelasticity model follows the concept of multiplicative decomposition, as is custom in the field of plasticity.[39] This decomposition introduces an internal variable, which relaxes towards the current deformation. We will assume a single relaxation time, in the spirit of the classical Maxwell model. The relaxation time will be assumed to be a function of T_g/T, following our earlier observation of viscoelastic relaxation in carbohydrate polymers.[28] T_g/T is the ratio of the moisture-dependent glass transition temperature T_g and the actual temperature T. If $T \leq T_g$, materials effectively behave as hard elastic solids (like dried pasta) and as viscoelastic rubber-like materials if $T \gg T_g$. In this study, we are particularly interested in the evolution of the central pore as a function of drying temperature and relative humidity of drying air.

In the field of large deformation mechanics of hydrogels, there are few studies on similar problems as addressed in this paper. We are aware of the recent paper on cavitation in viscoplastic hydrogels.[40] Here, inertial effects are taken into account, but we expect that these are negligible for slow food

drying, which often contains pre-existing pores. Yet, interestingly this paper also links cavitation and fracturing.

2 Model description

2.1 Balance equations

The evolution of the pore inside the viscoelastic core–shell system during drying requires the simultaneous solution of the mass balance for the moisture, the momentum balance for calculating the stress, and the energy balance for the temperature. The mechanical energy created by deformation will be dissipated *via* viscoelastic relaxation. All equations hold for both the core and the shell material. They will differ only in material properties. The central pore is assumed to be filled with a mixture of air and water vapour. The air is assumed to be insoluble in the liquid water. The gas in the pore is treated as an ideal gas.

This problem of pore formation is a prime example of a multiphysics problem. In Fig. 1, we have indicated schematically the multiphysics coupling between the mass, momentum and energy balance equations, supplemented with the viscoelastic relaxation. With blue arrows we have indicated the coupling between the state variables, fluxes and potentials in various balance equations. In the caption of Fig. 1, all couplings are shortly described to give the reader a direct overview of the complexity. All equations and variables are further detailed below. In the Appendix section, one finds more details about
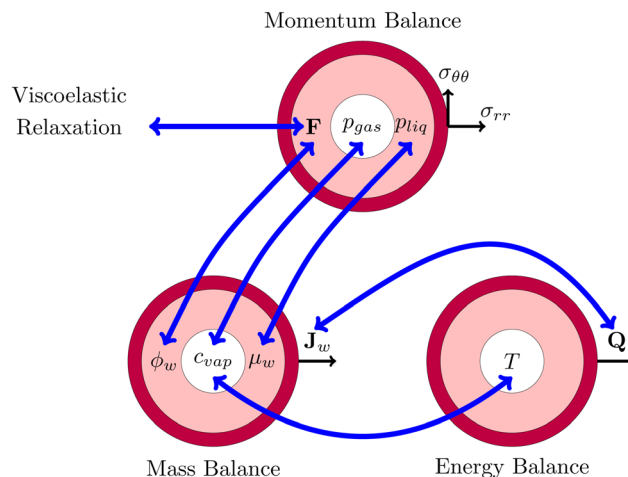

Fig. 1 Schematic representation of the multiphysics coupling in the model. During drying, there is heat and mass transfer *via* the fluxes $\mathbf{Q}$ and $\mathbf{J}_w$, increasing temperature T and lowering water volume fraction ϕ_w. The fluxes are coupled *via* evaporative cooling. The vapour concentration c_{vap} changes due to the temperature and the chemical potential (water activity) $\mu_w = R_{gas}T\log(a_w)$ of the shell. The decrease of moisture leads to deformation $\mathbf{F}$, leading to the development of stresses ($\sigma_{rr}, \sigma_{\theta\theta}$) and pressures p_{liq} and p_{gas}. The pressure in the gel p_{liq} couples back to the chemical potential μ_w, driving the mass fluxes $\mathbf{J}_w$. The gas pressure is mainly determined by changes in the vapour pressure $p_{vap} = c_{vap}/M_wR_{gas}T \approx a_w p_{sat}(T)$ and the stress in the core ($p_{gas} = -\sigma_{rr}(r_{in})$). Stresses also decrease *via* viscoelastic relaxation, modelled using the multiplication decomposition of the deformation $\mathbf{F}$.

solving the equations using the finite element method *via* the weak form.

First, we describe the governing equations for the reference frame, co-moving with the deforming polymer network. The time derivative is in terms of the material derivative: $D_t = \partial_t + \nabla \cdot \mathbf{v}_s$, where $\mathbf{v}_s$ is the velocity of the solid phase. The mass balance for the water in the core and the shell is:

$$D_t \phi_w = -\nabla \cdot \mathbf{j}_w = \nabla \cdot \frac{D_s \nu_w}{R_{gas} T} \nabla \mu_w \tag{1}$$

where ϕ_w is the volume fraction of water, $\mathbf{j}_w$ is the diffusive water flux given by generalized Fick's law, D_s is the self-diffusivity of water, ν_w is the molar volume of water, R_{gas} is the universal gas constant, and μ_w is the chemical potential (in units of [J m^{-3}]).

The chemical potential will have two contributions: one due to the mixing energy of water and biopolymers and another due to the elastic energy due to the deformation:[17]

$$\mu_w = \mu_{w,mix} + p_{liq} = -\Pi_{mix} + p_{liq} \tag{2}$$

The osmotic pressure Π_{mix} is the mixing contribution, and p_{liq} is the hydrostatic pressure in the solvent, resulting from the deformation. The mixing contribution follows the scaling law of Cloizeaux:[41]

$$\Pi_{mix} = \alpha G \tilde{\phi}^{\beta} \tag{3}$$

with $\beta = 9/4$ and $\tilde{\phi} = \phi_s/\phi_{ref}$, which is the ratio of the (current) polymer volume fraction, $\phi_s = 1 - \phi_w$, and the polymer volume fraction in the reference state, as defined below. α is a constant, defined in ref. 41, and G is the elastic modulus.

During dehydration/swelling of soft matter, one assumes that it is in a steady state:[17]

$$\nabla \cdot \sigma = 0 \tag{4}$$

where σ is the stress tensor, which follows from the thermodynamic theory of Suo.[17] For spherical geometries, the stress has only non-zero diagonal components, σ_{rr}, and $\sigma_{\theta\theta} = \sigma_{\phi\phi}$, which are formulated in terms of the stretches λ_i of the polymer network in the principal directions. These stretches are the eigenvalues of the deformation gradient tensor $\mathbf{F}$. For our spherical symmetry problem, $\mathbf{F}$ is a diagonal tensor. The stretch parameters are related under the incompressibility conditions:

$$\tilde{\phi} \lambda_r \lambda_\theta^2 = 1 \tag{5}$$

It is convenient to define the swelling factor $J = \lambda_r \lambda_\theta^2 = \det(\mathbf{F})$. With $\tilde{\phi} = \phi_s/\phi_{ref}$, which is the ratio of the (current) polymer volume fraction, $\phi_s = 1 - \phi_w$, and the polymer volume fraction in the reference state, as defined below.

We follow the Neo-Hookean model for the stress components.[42] For pure elastic materials, the stress follows:

$$\sigma_{ii} = \tilde{\phi} G \lambda_i^2 - p_{liq} \tag{6}$$

Below, we will give the stress relationships for viscoelastic materials.

The energy balance reads:[43]

$$D_t C_{eff} T = -\nabla \cdot \mathbf{Q} \tag{7}$$

where C_{eff} is the volumetric heat capacity, which changes due to moisture transfer.[43] Hence,

$$C_{eff} = \phi_w C_w + \phi_s C_s \tag{8}$$

with C_i as the volumetric heat capacity of each phase.

The heat flux $\mathbf{Q}$ follows:[44]

$$\mathbf{Q} = -k\nabla T + C_w \mathbf{j}_w T \tag{9}$$

The first contribution accounts for heat conduction, and the second contribution accounts for the convection of heat by the water flow, which has the volumetric heat capacity C_w. The latter contribution is often neglected in studies concerning thermosensitive hydrogels,[45–47] but it is correctly described in ref. 43 and 44.

We assume that the thermal conductivity k is a simple volume average:[48]

$$k = \phi_w k_w + \phi_s k_s \tag{10}$$

where k_i is the thermal conductivity of each phase.

For viscoelastic relaxation, we follow, ref. 49 where the deformation gradient is decomposed in an elastic and viscous contribution:

$$\mathbf{F} = \mathbf{F}_e \mathbf{F}_v \tag{11}$$

$\det(\mathbf{F}_e) = J_e = J$, $\det(\mathbf{F}_v) = J_v = 1$. Furthermore, we define the internal variable as:

$$A = 1/\lambda_{\theta,v}^2 = \lambda_{r,v} \tag{12}$$

which is related to the eigenvalues of $\mathbf{F}_v$, *i.e.* the stretch parameter $\lambda_{r,v}$. Also, we define the elastic stretch parameter as:

$$\lambda_{\theta,e}^2 = \lambda_\theta^2/A \tag{13}$$

where $\lambda_{\theta,e}$ is one of the eigenvalues of $\mathbf{F}_e$.

The internal variable evolves following a single relaxation time scheme:

$$\frac{dA}{dt} = \frac{1}{\tau}\left(\frac{1}{\lambda_\theta^2} - A\right) \tag{14}$$

where τ is the relaxation time.

The principal components of the stress can be rewritten as:

$$\sigma_{\theta\theta} = \frac{G}{J_e}\lambda_\theta^2 A - p$$
$$\sigma_{rr} = \frac{G}{J_e}\frac{1}{\lambda_\theta^4 A^2} - p \tag{15}$$

Thus, *via* viscoelastic relaxation $\lambda_{\theta,e}^2 = \lambda_\theta^2 A$ will evolve towards unity, *i.e.* a stress-free state.

2.2 Boundary conditions

For the mass balance, we use Robin-type boundary conditions. At the inner boundary, at $r = r_{in}$, it holds:

$$\mathbf{j}_w \cdot \hat{\mathbf{n}}(r_{in}) = -j_{cav} = -\frac{\beta_{cav}}{M_w}[a_w(r_{in}) - RH_{cav}]c_{sat}(T_{gas}) \tag{16}$$

where $a_w(r_{in})$ is the water activity, related to the chemical potential of the hydrogel at the inner boundary via $\mu_w(r_{in}) = R_{gas}T_p \log(a_w)$. RH_{cav} is the relative humidity of the gas inside the pore, related to the vapour pressure via $RH_{cav} = p_{vap}/p_{sat}(T_{gas})$, where $p_{sat}(T)$ is the saturated vapour pressure at temperature T. The gas temperature is assumed equal to the product temperature: $T_{gas} = T_p(r_{in})$. $c_{sat}(T) = M_w p_{sat}(T)/R_{gas}T$ is the saturated vapour concentration (in kg m^{-3}). M_w is the molar mass of water. $\beta_{cav} = D_{air}/(r_{in}/5)$ is the mass transfer coefficient for water transport inside the pore. $r_{in}/5$ is the characteristic diffusion length.[50]

At the outer boundary, at $r = r_{out}$, the mass flux reads:

$$\mathbf{j}_w \cdot \hat{\mathbf{n}}(r_{out}) = +j_{evap} = \frac{\beta_{air}}{M_w}\left[a_{w,ext}c_{sat}(T_p) - RH_{ext}c_{sat}(T_{ext})\right] \quad (17)$$

where $\beta_{air} = h_{air}/\rho_{air}c_{p,air}$ is the mass transfer coefficient of the external boundary layer, and following the Lewis relationship, it is linear with the heat transfer coefficient of the boundary layer h_{air}. $\rho_{air}c_{p,air}$ is the volumetric heat capacity of air. The water activity at the outer surface is defined by $\mu_w(r_{out}) = R_{gas}T_p \log(a_{w,ext})$. RH_{ext} is the external relative humidity, and T_{ext} is the temperature of the drying air, both of which are process settings of the drying process.

For the momentum balance, we impose pressures at the outer and inner boundaries:

$$\sigma_{rr}(r_{out}) = p_0; \quad \sigma_{rr}(r_{in}) = p_{gas} \quad (18)$$

The gas pressure p_{gas} is the sum of the partial air and water pressures:

$$p_{gas} = p_{air} + p_{vap} \quad (19)$$

As the number of moles of air N_{air} remains constant, we have:

$$N_{air} = \frac{p_{air,0}V_{gas,0}}{R_{gas}T_{init}} = \frac{p_{air}V_{gas}}{R_{gas}T_{gas}} \quad (20)$$

where $p_{air,0} = p_0 - p_{sat}(T_{init})$ is the initial air pressure, $V_{gas,0} = 4/3\pi R_{in}^3$ is the initial pore volume, T_{init} is the initial product temperature, $V_{gas} = 4/3\pi r_{in}^3$ is the actual pore volume. R_{in} is the initial pore radius, and p_0 is the ambient pressure.

The partial water vapour pressure follows:

$$p_{vap}V_{gas} = N_{vap}R_{gas}T_{gas} \quad (21)$$

with

$$\frac{dN_{vap}}{dt} = j_{cav}4\pi r_{in}^2 \quad (22)$$

which will be integrated during simulations to obtain N_{vap}.

The boundary condition for the heat flux at the outer boundary is:

$$\mathbf{Q} \cdot \hat{\mathbf{n}}(r_{out}) = +Q_{evap} = h_{air}(T_p - T_{ext}) + j_{evap}\Delta H_{evap} \quad (23)$$

where ΔH_{evap} is the heat of evaporation, expressed in J mol^{-1}.

At the inner boundary, we assume that the gas temperature is equal to the product temperature, and hence:

$$\partial_r T_p(r_{in}) = 0 \quad (24)$$

The model is implemented via the finite element method, using COMSOL. As common in models developed by Suo, we have formulated the model in the weak form. As this formalism is not commonplace in food science, we describe in the Appendix section the weak forms of the above equations and boundary conditions (if required).

2.3 Self-diffusion coefficient

Comparing the Darken relationship, the self-diffusion coefficient has a contribution for solutes $D_{s,s}$ and water $D_{s,w}$:

$$D_s = \phi_w D_{s,s} + \phi_s D_{s,w} \quad (25)$$

The latter will follow the free-volume theory,[51] which we assume to hold universally for (hydrophilic) food materials. It has been validated for sugar solutions and maltodextrins.[51–53] For aqueous solutions, $D_{s,s}$ would follow the generalized Stokes–Einstein equation, but a biopolymer network cannot be represented as a solute. Hence, we follow the (modified) relationship by Tokita:[11,54]

$$D_{s,s} = D_{w,0}\frac{\phi_{s,lim}}{\phi_{s,lim} + \phi_s^{3/2}} \quad (26)$$

In this modified Tokita relationship, we have matched two asymptotics: (a) for $\phi_s \to 0$, it approaches the water self-diffusion (in water) $D_{s,s} \to D_{w,0}$, and (b) for $\phi_s \gg 0$, it follows the original Tokita scaling $D_{s,s} \sim \phi_s^{-3/2}$. $\phi_{s,lim} \approx 0.03$ is an arbitrary small number. Thus, the modified Tokita relationship avoids the singularity of the original theory at $\phi_s = 0$.

The free-volume theory states:

$$\ln\left(\frac{D_{s,w}}{D_{w,0}}\right) = -\frac{\Delta E}{R_{gas}T} - \gamma\frac{V_{cr}}{V_f} \quad (27)$$

where ΔE is an activation energy, V_f is the free volume, and V_{cr} is a kind of "activation volume". In the maltodextrin sorption paper, we modified our original theory (in ref. 51), to account for the fact that the derivative of the free volume with ϕ_s shows a discontinuity at the glass transition (which remains rather constant, leading to a plateau in $_{s,w}$, which is consistent with ref. 55). Although the parameters for the free volume theory are taken for sucrose, cf.,[56] it is shown that this relationship holds for any polysaccharide – independent of its molecular weight.[51–53,57]

2.4 Viscoelastic relaxation times

The viscoelastic relaxation times related to α-relaxation are assumed to depend on T_g/T, as we have found for starches and maltodextrins.[28] For wet food materials, like fresh vegetables, $T_g/T \approx 0.5$ and the viscoelastic relaxation times can be quite short, which can make the required time step quite short, and computation times quite long. To avoid this situation, we assume in series with the α-relaxation another Maxwellian relaxation process with a constant relaxation time τ_M:

$$\tau = \tau_M + \tau_\alpha(T_g/T) \quad (28)$$

For nearly elastic skins, the viscoelastic relaxations are relatively slow, with $\tau_M \sim 10^3 \cdots 10^4$ s. For viscoelastic hydrogels, the relaxation is assumed to be quite fast, with $\tau_M \sim 10^{-1} \cdots 10$ s.[14,15] For starch and maltodextrins, the logarithm of the relaxation time scales is linear with T_g/T:

$$\log(\tau_\alpha) \sim \frac{T_g}{T} \qquad (29)$$

which can be viewed as a generalization of the Arrhenius relationship. In the glassy state, where $T_g/T > 1$ the food materials are assumed to be practically behaving as elastic solids.

T_g is a function of the moisture content, as captured by the Couchman–Karasz relationship:

$$T_g = \frac{y_w T_{g,w} \Delta c_{p,w} + y_s T_{g,s} \Delta c_{p,s}}{y_w \Delta c_{p,w} + y_s \Delta c_{p,s}} \qquad (30)$$

where y_i is the mass fraction of component i, $T_{g,i}$ is its glass transition, and $\Delta c_{p,i}$ is its change in heat capacity at the glass transition.

3 Results

First, we have performed simulations for a nearly elastic system, such that the reader gets an impression of the system behaviour following our previous model. Results are shown in Fig. 2. Simulations are performed for $R_{in}/R_{out} = 0.35$, $G_{skin}/G_{core} = 20$, $\tau_{core} = 10^4$ s, and $\tau_{skin} = 10^7$ s. $t_e = 10\tau_{skin}$. If the elastic skin has a sufficient high elastic modulus ($G_{skin}/G_{core} = 20$), we observe that there is a significant amount of pore opening: $r_{in}(t_e) > R_{in}$. The larger the external osmotic pressure Π_{ext} the larger the pore opening.

There are interesting dynamics in this problem. A quasi-steady state is obtained if the drying front has reached the inner pore, which is indicated by the moment that the vapour pressure reaches its final value. At this time, the outer radius is showing a minimal value. After this moment, the inner radius shows a further increase, due to the loss of moisture, but the external radius increases slowly. If most of the moisture is removed, the system enters a quasi-steady state, with stable pressures and inner/outer radii. However, due to the very long viscoelastic relaxation times, we observe a decrease in gas and air pressures and a concomitant decrease in the radii. As in the purely elastic case, the Finite element solver becomes unstable for $\Pi_{ext}/G_{core} \geq 2000$.

Subsequently, we have lowered the relaxation times to $\tau_{core} = 10^2$ s, and $\tau_{skin} = \{10^3, 10^5\}$ s. We compare the response, as shown in Fig. 3, with the previous calculation. We observe that, for short times, the behaviour is comparable to the nearly elastic system, but with a lowered gas pressure and an increased pore size. However, at longer times, the mechanical stresses are relaxed, and the total gas and air pressures return to equilibrium values: *i.e.* the ambient pressure p_0. Also, the pore radius decreases to an equilibrium value, which is independent of Π_{ext}, but is probably determined by the amount of air and the final temperature. Of course, the return to
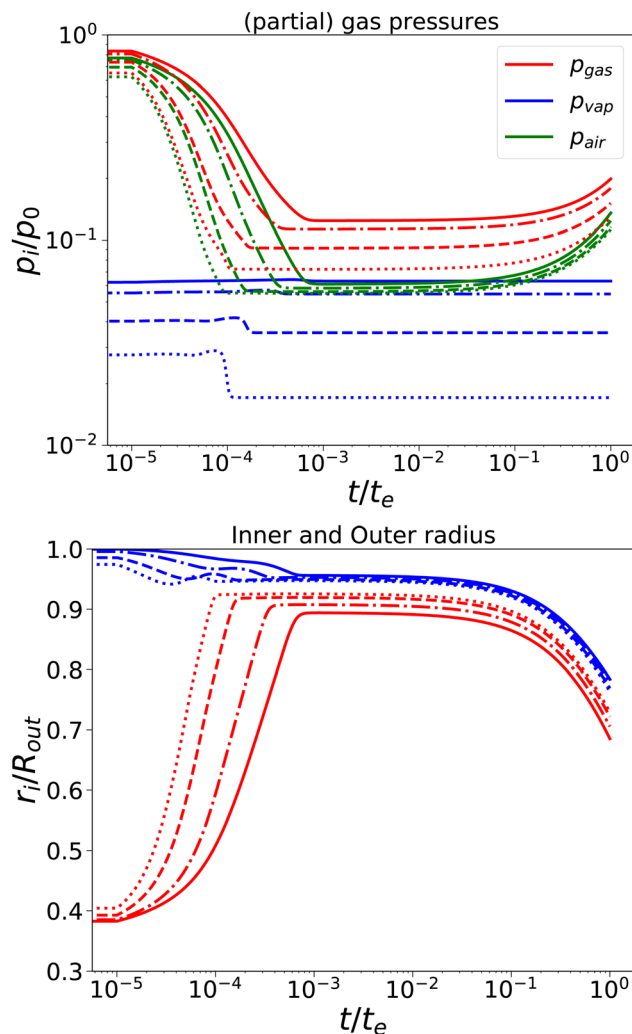

Fig. 2 Changes in (a) the (partial) gas pressures (top pane) and the inner and outer radii for a nearly elastic skinned hydrogel with the central pore and (b) the inner (red line) and outer radii (blue lines) of the system (bottom pane). The system was subject to external pressures $\Pi_{ext}/G_{core} = \{100, 200, 500, 1000\}$ (plotted with linstyles '–', '-.', '−', ':'). $R_{in}/R_{out} = 0.35$, and $G_{skin}/G_{core} = 20$.

equilibrium is shorter if $\tau_{skin} = 10^3$ s. Still, we observe numerical instability if $\Pi_{ext}/G_{core} \geq 2000$.

For high-moisture food materials like fruits and vegetables, having lost turgor, the (main) viscoelastic relaxation times are in the order of 1 s.[58–60] Food materials have a distribution of relaxation times, but we will take the simplifying assumption of only a single relaxation time, which is temperature and moisture-dependent. We assumed the following relationship for τ_α:

$$\tau_\alpha = \frac{\eta_0(T_g/T)}{G_\infty} \qquad (31)$$

where η_0 is the zero shear viscosity of the biopolymeric matrix, and G_∞ is the value of elastic modulus biopolymers attained in the glassy state. For values of η_0, we follow the relationship we have found earlier for starch.[28] For biopolymers, we typically find $G_\infty = 10^8 \cdots 10^{10}$ Pa.[28,29,61,62] For our simulations, we
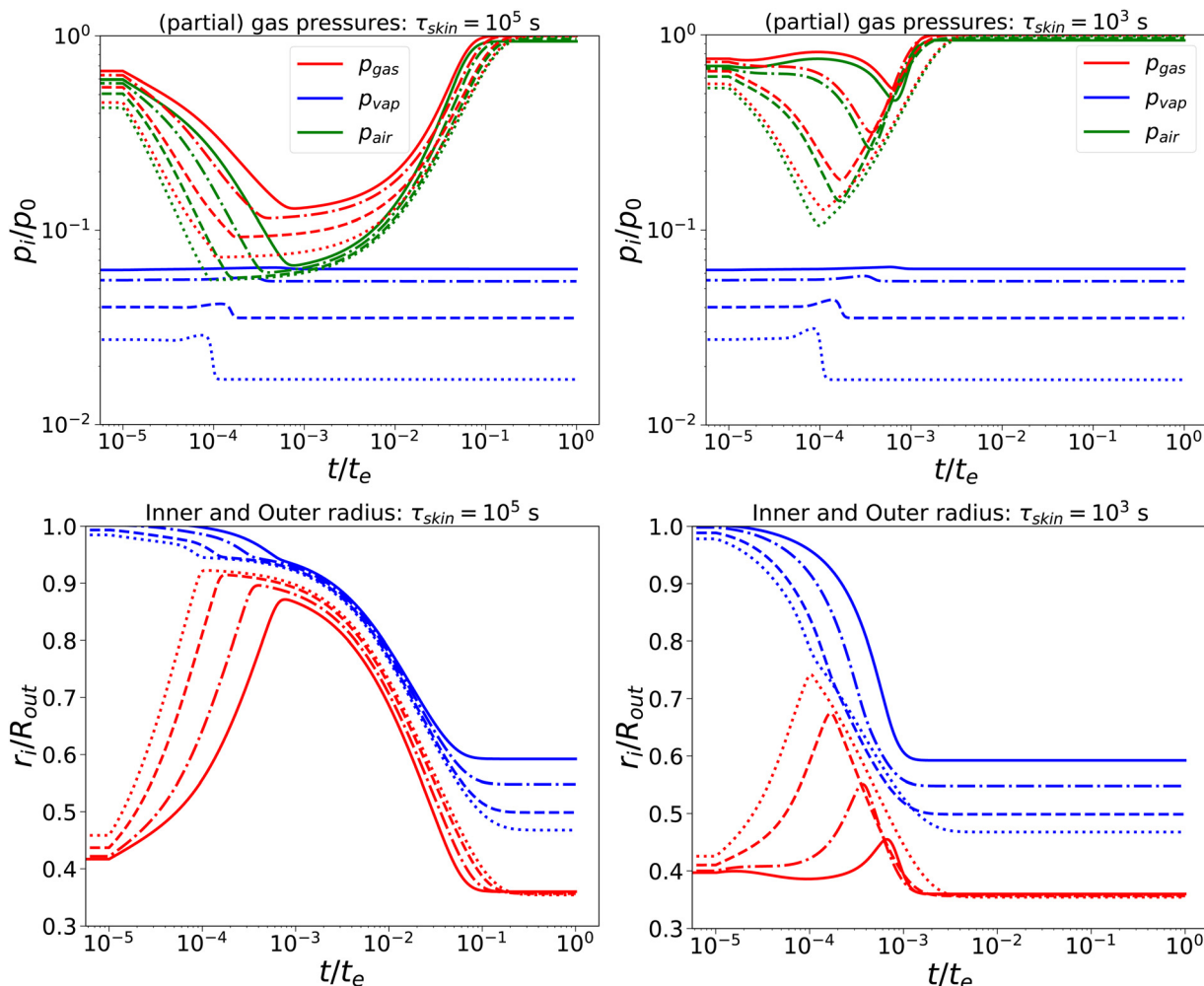
Fig. 3 Changes in (a) the (partial) gas pressures (top pane) and inner and outer radii (bottom pane) for a nearly elastic skinned hydrogel with the central pore, and (b) the inner (red line) and outer radii (blue lines) of the system for $\tau_{skin}\{10^3, 10^5\}$ s (left and right) and τ_{core} = 100 s, Π_{ext}/G_{core} = {100, 200, 500, 1000} (plotted with linstyles '-', '-.', '−', ':'). R_{in}/R_{out} = 0.35, and G_{skin}/G_{core} = 20.

assumed the maximal value: G_∞ = 10 GPa, rendering $\tau_\alpha \approx 1$ at $T_g/T = 1$.

With a short relaxation time of 1 s, we expect that there is no initial pore growth, but only in the late stage of drying, if the skin enters into the glassy state, provided sufficient low external osmotic pressure Π_{ext}. Furthermore, we take an initial pore size more in line with actual pore sizes in fresh fruits and vegetables. Results are shown in Fig. 4, for simulations with τ_{core} = τ_{skin} = 1 s, R_{in}/R_{out} = 0.01, G_{skin}/G_{core} = 20, and Π_{ext}/G_{core} = {100, 500, 1000, 1500}. We note that the upper bound of Π_{ext}/G_{core} is limited by numerical stability, but calculations show that under these conditions $a_w \approx 0.1$,[12] which is below the target of most food drying processes ($a_w \approx 0.2$). Hence, the upper bound is also a practical limit.

We observe that the pore opening only occurs if it holds for the skin that $T_g/T > 1.1$. The pore opening occurs relatively suddenly, and it grows to a size about 50 times its original size. Such cavitation events have been observed for spray drying of food material droplets.[1,4,63–66]

In other cases, the relaxation times τ remain within the time scale of drying $\tau \ll t_e$, allowing stresses to relax away. If $T_g/T > 1.1$, the relaxation time of the skin becomes $\tau/t_e \gg 10^3$, meaning that it has become purely elastic. In the skin, the elastic stresses become frozen-in, leading to a difference in ϕ_s between the core and the skin. In the core, $\tau \sim 10^4$ s, meaning that viscoelastic stresses still can be relaxed away.

As an illustration of the sudden transition in pore opening, we have performed a more detailed parameter study where we have varied external osmotic pressures Π_{ext} around the transition T_g/T. In Fig. 5, we show how the final radii of the pore and the skin ($r_{in,\infty}$ and $r_{out,\infty}$) vary with the final value of T_g/T of the skin. We observe that at values $T_g/T \le 1.1$ the pore radius remains small, and the outer radius shrinks with increasing external osmotic pressure. However, if $T_g/T > 1.1$, we observe an increase in the final pore radius, approaching an asymptotic value at $T_g/T = 1.5$. Concomitantly, the pore inflation leads to an increase of the outer pore radius at increasing T_g/T values.
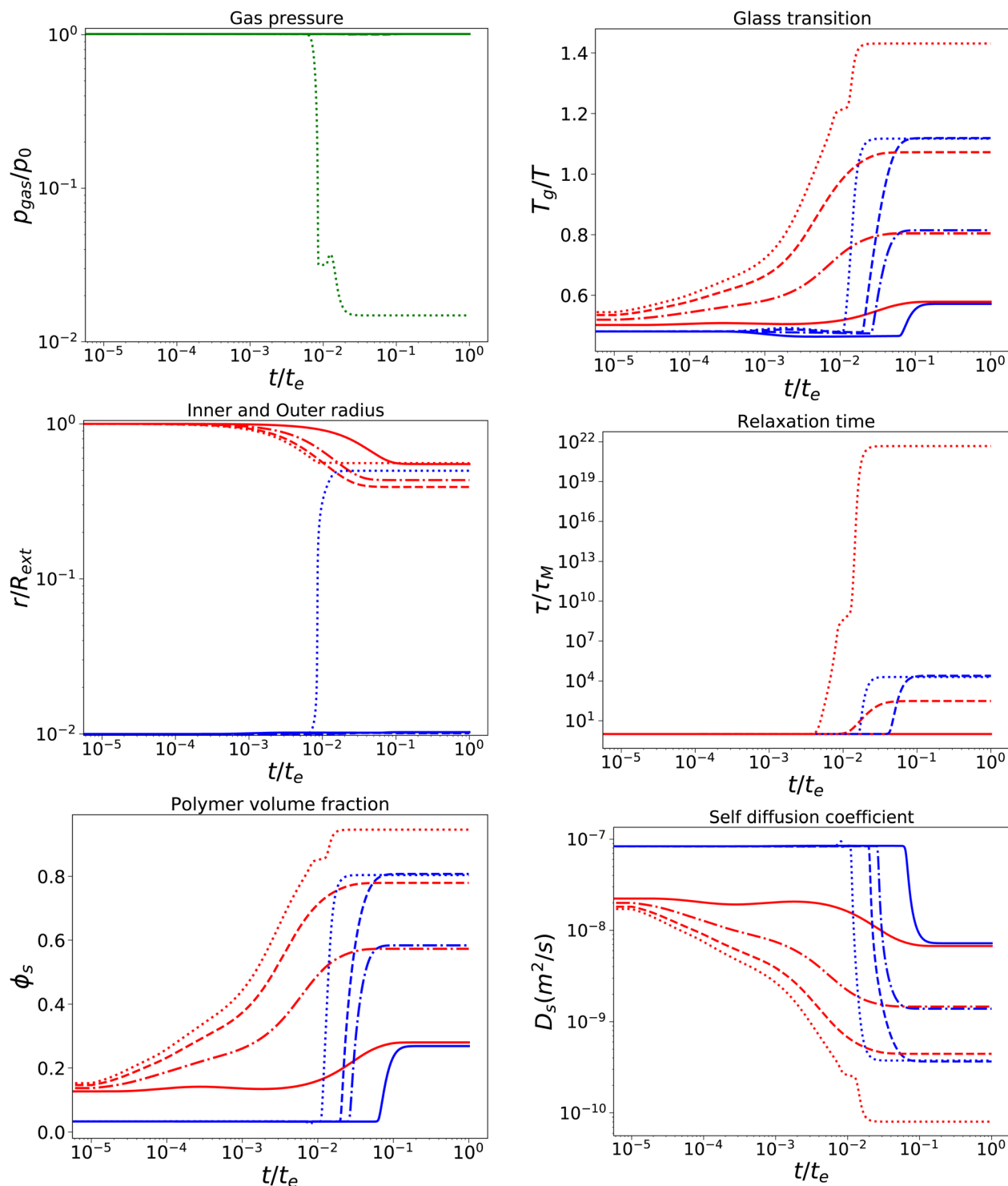
Fig. 4 Changes in various state parameters and material properties in the outer skin surface (solid lines) and inner cavity surface (dashed lines) as a function of time for a series of external osmotic pressures $\Pi_{\text{ext}}/G_{\text{core}} = \{500, 1000, 1500, 1900\}$ (plotted with linstyles '-', '-.', '--', ':'). The properties of the core are indicated in blue, while the skin properties are indicated in red. Simulations are performed for $\tau_{\text{core}} = \tau_{\text{skin}} = 1$ s, $R_{\text{in}}/R_{\text{out}} = 0.01$, and $G_{\text{skin}}/G_{\text{core}} = 20$.

The temporal evolution of stress profiles for the case $\Pi_{\text{ext}}/G_{\text{core}} = 1500$ is shown in Fig. 6. At early times $t/t_e < 10^{-2}$, there is little stress build-up due to fast viscoelastic relaxation times. At $t/t_e = 10^{-2}$, the skin enters into a glassy state, with long relaxation times, leading to a strong build-up of stresses. At later times $t/t_e > 10^{-2}$, the (nearly) glassy core also develops stresses, which are not relaxed away. Especially at the pore, the stress drops below $-p_0$, causing the gas in the pore to
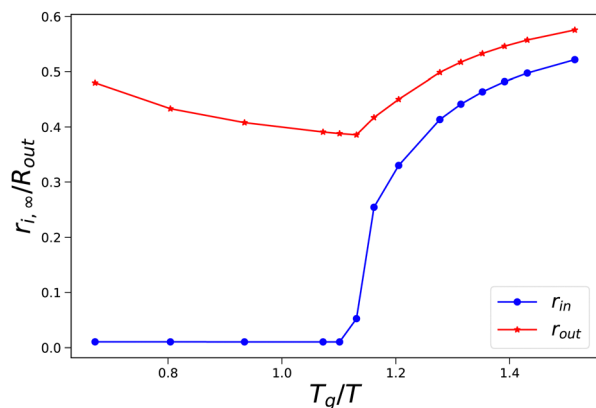
Fig. 5 Final pore radius r_{in} and skin radius r_{out} at the end of drying as a function of the (final) T_g/T value of the skin. Simulations are performed with $R_{in}/R_{out} = 0.01$, and $500 \leq \Pi_{ext}/G_{core} \leq 1900$.
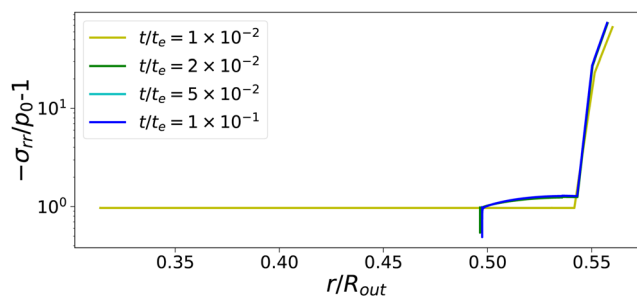

Fig. 6 Profiles of stress component σ_{rr} at various times for $\Pi_{ext}/G_{core} = 1500$. If the skin enters into the glassy state, $t/t_e > 10^{-2}$, the central the pore opens suddenly. First stresses develop in the glassy skin and later in the (nearly) glassy core, leading to $-\sigma_{rr}(r_{in}) \ll p_0$, inflating the central pore.

expand. The changes in stress profiles and the pore opening develop indeed vary suddenly. After the pore opening, the stress profiles do not change anymore.

4 Conclusions

In this paper, we have studied numerically the pore formation during the drying of a spherical viscoelastic core–shell system with a central gas-filled cavity, which approximates food materials like vegetables and fruits. For these materials, it is known that porosity increases during drying after the event of case hardening, *i.e.* the formation of a hard, elastic skin.[10] Case hardening occurs if the dried material enters into the glassy state. A similar mechanism we have observed for the (idealized) viscoelastic core–shell system, with viscoelastic relaxation times depending on the ratio of T_g/T. When the material remains in the rubbery state, the viscoelastic relaxation times are short, and there is a little change in the pore size, or it can even be somewhat compressed. If the skin enters the glassy state, the relaxation times become so large that stresses cannot be relaxed away on the practical time scale of the food drying. The developed stresses prevent the skin from further shrinkage, and stresses develop also in the core upon further drying and

shrinkage of the core material. Eventually, the stresses at the surface of the cavity lead to gas pressures significantly lower than the atmospheric pressure, leading to inflation of the pore.

Important for the modelling of the pore formation is the multiphysics coupling between the heat, momentum, mass transfer, and the material properties. Here we go beyond the current state-of-the-art food drying models, which are represented by the multiphysics models of Datta and coworkers.[10,67] Similar to our model, Datta and coworkers have introduced large deformation mechanics, coupled to heat and mass transfer. Their models can model porosity development during intensive heating like baking, frying, or microwaving.[67] Yet, their models lack the viscoelastic nature of food materials in the rubbery state, and there is no coupling of the stress to the driving force for mass transfer, *i.e.* the chemical potential. However, their framework is easily extended to incorporate the above features.

Our modelling results also have a strong resemblance with the cavity formation during (spray) the drying of droplets made of soft (food) materials.[4,68] Also, here the formation of a rigid skin is said to be crucial for the cavity formation. The cavity can grow relatively large, leading to hollow particles with a thin shell. This morphology strongly resembles the morphology of our viscoelastic system, if subjected to drying conditions bringing the skin in the glassy state. Large pore formation is also observed during microwave puffing of food materials, where a large pore (blister) is surrounded by a thin (porous) crust.[69] The cavity formation in drying droplets of soft matter solutions has been modelled.[30] However, it was assumed that the material becomes elastic beyond a critical gelation concentration. Below that critical point drying is modelled *via* the common Fick model. While there is a coupling of elastic stress to the driving force of mass transfer, the model lacks viscoelasticity. Incorporating viscoelasticity avoids this discrete change of modelling and material properties at the critical concentration. Viscoelasticity is important if skin formation is *via* gelation. A transient large bubble can be formed, but at a later stage of drying, if the glassy state is not reached, the hollow particle can undergo either invagination[70] or buckling and collapse.[71] This collapse is also observed in our simulations if the materials are sufficiently elastic to stresses, but viscoelastic relaxation times are not long enough to maintain the expanded pore, as shown in Fig. 3, because we assume that the spherical geometry our model cannot show buckling. However, the modelling framework developed by Suo and coworkers, which we have followed here, has been used for the study of buckling of soft materials with a stiff skin.[72–75] Of course, for describing buckling it requires 3D models.[76]

Hence, we think that the proposed modelling framework of Suo, extended with non-linear viscoelasticity, is the appropriate method for modelling the intricate three-dimensional deformation and structure formation during (spray) drying of food materials. However, realistic simulations of these phenomena require good knowledge of their rheological properties: how viscoelastic relaxation times and elastic loss moduli depend on the temperature and moisture content. We should note that

many real food materials like vegetables and polysaccharides show a broad distribution of multiple relaxation times.[14,15,26,28,77] This requires a generalization of the multimode Maxwell model. Recently, we have developed a first simple model along these lines,[29] which explains the hysteresis during moisture sorption of maltodextrins. The model proposed in this paper can easily be expanded to a multimode approach by introducing multiple internal variables $\mathbf{A_i}$ for each viscoelastic relaxation mode. Each model will have its own relaxation time τ_i and elastic modulus G_i. Hence, in our future research, we will extend the presented model towards 3D, and include multiple relaxation modes.

Author contributions

Ruud van der Sman conceptualized and drafted the paper. Theory and model development was performed by all authors. Ruud van der Sman and Luciano Teresi reviewed and edited the paper.

Conflicts of interest

There are no conflicts to declare.

Appendix: weak forms in the material frame

In the mechanics of hydrogels, it is common to formulate the problem in a non-moving material frame.[16] The stretch parameters are computed concerning this static material frame, which we denote below as the domain frame. Typically, the dry configuration is chosen as this domain frame. However, as we have a bilayer material (core–shell material), that is stress-free, fully relaxed, and uniformly swollen in the initial state, it can be proven that a dry configuration with zero stress and uniform deformation is physically not realizable. Hence, for our problem, it is more convenient to use the initial state as the domain frame, which we characterize with coordinates $\mathbf{X}$.

In the general case, the deformation described in terms of the deformation gradient tensor $\mathbf{F}$:[16]

$$F_{ij} = \frac{\partial x_i(\mathbf{X}, t)}{\partial X_j} \tag{32}$$

where $\mathbf{x}$ is the coordinate of a material point in the current deformed state, and $\mathbf{X}$ is its position in the domain state. By our choice of the initial state as the domain frame, we have shown that in this case the deformation gradient tensor equals the identity matrix $\mathbf{F} = \mathbf{I}$. Yet, above we have stated that the hydrogel in the initial state is fully relaxed, thus $\mathbf{F_e} = \mathbf{I}$, and $\mathbf{F_v} = \mathbf{I}$.

$$\mathbf{F} = \mathbf{F_v}\mathbf{F_e} \tag{33}$$

The viscoelastic relaxations define an intermediate stress-free configuration, from which one computes the elastic deformation. It should be noted that the core and the shell will have intermedia configurations, as they differ in viscoelastic
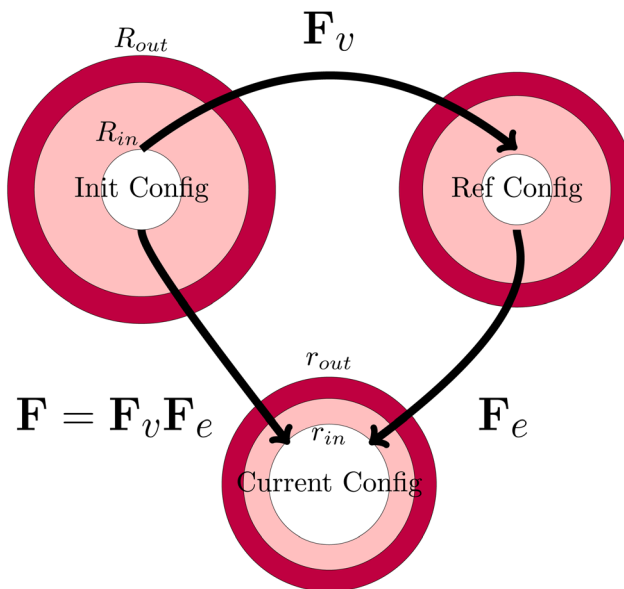

Fig. 7 Definition of the various configurations for defining the deformation. The initial configuration is used as the domain frame, defining the deformation $\mathbf{F}$ to the current (deformed) configuration. The elastic deformation $\mathbf{F_e}$ is defined as the intermediate reference configuration. It should be noted that, in all 3 configurations, the skin and the core have matching deformations at their interface.

properties. This multiplicative decomposition and its connection to the three defined coordinate frames is nicely illustrated in Fig. 7.

We extend the incompressibility condition also towards the initial frame, where the control volume is characterized by radius r_0, thickness $\mathrm{d}r_0$, and volume fraction ϕ_0:

$$\phi_0 r_0^2 \mathrm{d}r_0 = \phi_s r^2 \mathrm{d}r = \phi_{\mathrm{ref}} R^2 \mathrm{d}R \tag{34}$$

We define $\Lambda_\theta = r/r_0$, $\lambda_\theta = r/r_{\mathrm{ref}}$, $\Lambda_\mathrm{r} = \mathrm{d}r/\mathrm{d}r_0$, $\lambda_\mathrm{r} = \mathrm{d}r/\mathrm{d}r_{\mathrm{ref}}$, $J_\mathrm{e} = \phi_{\mathrm{ref}}/\phi_\mathrm{s}$, $J_0 = \lambda_0^3 = \phi_{\mathrm{ref}}/\phi_0$, $J_\mathrm{d} = \phi_0/\phi_\mathrm{s}$ and hence:

$$J_\mathrm{d}^{-1}\Lambda_\theta^2\Lambda_\mathrm{r} = J_\mathrm{e}^{-1}\lambda_\theta^2\lambda_\mathrm{r} = J_0^{-1}\lambda_0^3 = 1 \tag{35}$$

The elastic stretch parameters $\lambda_{\mathrm{e,i}}$ are related to the eigenvalues of the (elastic) Cauchy tensor (which removes any contribution from the solid body rotation):

$$\mathbf{C_e} = \mathbf{F}_\mathrm{e}^T\mathbf{F_e} \tag{36}$$

The eigenvalues of $\mathbf{C_e}$ are $\lambda_{\mathrm{e,i}}^2$.

The momentum balance in the material frame is formulated in terms of the first Piola stress tensor $\mathbf{S}$:

$$\nabla_X \cdot \mathbf{S} = 0 \tag{37}$$

where ∇_X is differentiation concerning the material frame. The Piola stress is related to true stress *via* a pull-back:

$$\mathbf{S} = \sigma\mathbf{F}^\star \tag{38}$$

with the conjugate:

$$\mathbf{F}^\star = J\mathbf{F}^{-T} \tag{39}$$

$J = \det(\mathbf{F}) = \lambda_\theta^2\lambda_\mathrm{r}$.

The following relationship holds for the true stress for viscoelastic materials:[49]

$$s = \frac{G}{J_e}\mathbf{F}_e\mathbf{F}_e^T - p_{\text{liq}}\mathbf{I} \tag{40}$$

Using $J_e = \lambda_{\theta,e}{}^2\lambda_{r,e}$, the Piola stress in components follows:

$$S_{rr} = G\frac{\lambda_{\theta,v}{}^2}{\lambda_{r,e}} - p_{\text{liq}}\lambda_{\theta}{}^2$$
$$\tag{41}$$
$$S_{\theta\theta} = G\lambda_{\theta}\lambda_{r,v} - p_{\text{liq}}\lambda_{\theta}\lambda_r$$

The momentum balance in spherical coordinates reads:

$$\partial_R S_{rr} + \frac{2}{R}(S_{rr} + S_{\theta\theta}) \tag{42}$$

The weak form is:

$$\int -\left[S_{rr}(\partial_R\tilde{u}) + \frac{2}{R}S_{\theta\theta}\tilde{u}\right]4\pi R^2 \mathrm{d}R \tag{43}$$

where $\tilde{u}$ is the test function, related to the stretch parameters: $\lambda_{\theta} = 1 + u/R$, $\lambda_r = 1 + \partial u/\partial R$. Below, we will indicate other test functions also with the tilde symbol.

The boundary conditions are also formulated in the weak form. For the inner boundary, it holds:

$$\int +p_{\text{gas}}\lambda_{\theta}{}^2\tilde{u}4\pi R^2 \mathrm{d}R \tag{44}$$

and for the outer boundary:

$$\int -p_0\lambda_{\theta}{}^2\tilde{u}4\pi R^2 \mathrm{d}R \tag{45}$$

The liquid pressure p_{liq} follows from the incompressibility condition:

$$J = \lambda_{\theta}{}^2\lambda_r$$
$$\hat{J} = \phi_{s,0} + \nu_w c \tag{46}$$
$$J = \hat{J}$$

where $\phi_{s,0}$ is the polymer volume fraction in the initial state, ν_w is the molar volume of water, and c is the moles of water per unit of volume in the domain frame. The volume fraction of water in the initial state is: $\phi_{w,0} = \nu_w c_0$. Hence, in the initial state $J = 1$. The pressure field is calculated as a Lagrangian multiplier to control the incompressibility condition via the weak form:

$$\int (J - \hat{J})\tilde{p}_{\text{liq}}4\pi R^2 \mathrm{d}R \tag{47}$$

The mass balance is formulated in terms of the state variable c as the number of moles of water per unit of volume of the domain (initial) configuration. The strong form of the mass balance in the material frame is:

$$\partial_t c = \partial_R N_{w,R} \tag{48}$$

The corresponding weak form is:

$$\int (\tilde{c}\partial_t c - N_{w,R}\partial_R\tilde{c})4\pi R^2 \mathrm{d}R \tag{49}$$

with the molar flux equal to:

$$N_{w,R} = -\frac{D_X}{R_{\text{gas}}T_p}\partial_R\mu_w \tag{50}$$

where D_X is the contravariant diffusion coefficient, which follows from the mapping from the current frame to the material frame.[12] It follows:

$$D_X = \frac{\lambda_{\theta}{}^2}{\lambda_r}D_s \tag{51}$$

In short, $\lambda_{\theta}{}^2$ accounts for changes in the surface area between the control volume, and λ_r corrects for changes in the thickness of control volumes.

The boundary conditions are implemented via the weak form. The inner boundary holds:

$$\int \lambda_{\theta}{}^2 j_{\text{cav}}\tilde{c}4\pi R^2 \mathrm{d}R \tag{52}$$

and the outer boundary holds:

$$\int \lambda_{\theta}{}^2 j_{\text{evap}}\tilde{c}4\pi R^2 \mathrm{d}R \tag{53}$$

The skin and the core have different elastic properties, and they will be treated as two different domains, each with their state variables c_{core} and c_{skin}. At their interface, the chemical potential should be continuous. We enforce this via the weak forms:

$$\int -(\mu_{w,\text{core}} - \mu_{w,\text{skin}})D_\mu\tilde{c}_{\text{core}}4\pi R^2 \mathrm{d}R \tag{54}$$

and

$$\int +(\mu_{w,\text{core}} - \mu_{w,\text{skin}})D_\mu\tilde{c}_{\text{skin}}4\pi R^2 \mathrm{d}R \tag{55}$$

where D_μ is a constant, determining the rate where this local equilibrium is enforced.

The weak form of the energy balance is:

$$\int (JC_{\text{eff}}\tilde{T}_p\partial_t T_p - \partial_R\tilde{T}_p Q_R)4\pi R^2 \mathrm{d}R \tag{56}$$

with the heat flux equal to:

$$Q_R = -k_X\partial_R T_p + N_{w,R}C_w T_p\nu_w \tag{57}$$

where $k_X = k\lambda_{\theta}{}^2/\lambda_r$ is the contravariant thermal conductivity.

The boundary conditions at the outer boundary in the weak form:

$$\int \lambda_{\theta}{}^2(h_{\text{air}}(T_p - T_{\text{ext}}) + j_{\text{evap}}\Delta H_{\text{evap}})4\pi R^2 \mathrm{d}R \tag{58}$$

At the inner boundary, we have the natural boundary conditions $\partial_R T_p = 0$, which does not require a weak form.

Finally, we note that the COMSOL model is available as ESI,† saved as a Java script, which can be uploaded into any version of COMSOL.

Notes and references

1 J. Bouman, P. Venema, R. J. de Vries, E. van der Linden and M. A. Schutyser, *Food Res. Int.*, 2016, **84**, 128–135.

2 T. K. Nguyen, S. Khalloufi, M. Mondor and C. Ratti, *Food Res. Int.*, 2018, **103**, 215–225.

3 E. Both, R. Boom and M. Schutyser, *Powder Technol.*, 2020, **363**, 519–524.

4 I. Siemons, R. Politiek, R. Boom, R. van der Sman and M. Schutyser, *Food Res. Int.*, 2020, **131**, 108988.

5 N. Zogzas, Z. Maroulis and D. Marinos-Kouris, *Drying Technol.*, 1994, **12**, 1653–1666.

6 V. Karathanos, N. Kanellopoulos and V. Belessiotis, *J. Food Eng.*, 1996, **29**, 167–183.

7 S. Khalloufi, A. Kharaghani, C. Almeida-Rivera, J. Nijsse, G. van Dalen and E. Tsotsas, *Trends Food Sci. Technol.*, 2015, **45**, 179–186.

8 M. U. Joardder, C. Kumar and M. Karim, *Crit. Rev. Food Sci. Nutr.*, 2018, **58**, 2896–2907.

9 I. Siemons, J. Veser, R. Boom, M. Schutyser and R. van der Sman, *Food Hydrocolloids*, 2022, **126**, 107442.

10 T. Gulati and A. K. Datta, *J. Food Eng.*, 2015, **166**, 119–138.

11 X. Jin and R. van der Sman, *Food Struct.*, 2022, **32**, 100269.

12 R. van der Sman, M. Curatolo and L. Teresi, *Curr. Res. Food Sci.*, 2024, 100762.

13 R. Van der Sman, E. Paudel, A. Voda and S. Khalloufi, *Food Res. Int.*, 2013, **54**, 804–811.

14 O. K. Ozturk and P. Singh Takhar, *Drying Technol.*, 2019, **37**, 1833–1843.

15 O. K. Ozturk and P. S. Takhar, *J. Texture Stud.*, 2020, **51**, 532–541.

16 W. Hong, X. Zhao, J. Zhou and Z. Suo, *J. Mech. Phys. Solids*, 2008, **56**, 1779–1793.

17 W. Hong, Z. Liu and Z. Suo, *Int. J. Solids Struct.*, 2009, **46**, 3282–3289.

18 W. M. Lai, J. Hou and V. C. Mow, *J. Biomech. Eng.*, 1991, **113**, 245–258.

19 J. M. Huyghe and J. D. Janssen, *Int. J. Eng. Sci.*, 1997, **35**, 793–802.

20 S. Achanta, M. R. Okos, J. H. Cushman and D. P. Kessler, *AIChE J.*, 1997, **43**, 2112–2122.

21 P. P. Singh, J. H. Cushman and D. E. Maier, *Chem. Eng. Sci.*, 2003, **58**, 2409–2419.

22 R. Van der Sman and A. Van der Goot, *Soft Matter*, 2009, **5**, 501–510.

23 X. Li, J. Bi, X. Jin, J. Lyu, X. Wu, B. Li and X. Li, *J. Food Eng.*, 2021, **293**, 110379.

24 R. Van der Sman and J. Broeze, *J. Phys.: Condens. Matter*, 2014, **26**, 464103.

25 L. Hu, J. Bi, X. Jin, Y. Qiu and R. van der Sman, *Foods*, 2021, **10**, 769.

26 I. Siemons, J. Veser, R. Boom, M. Schutyser and R. van der Sman, *Food Hydrocolloids*, 2022, 107442.

27 L. Hu, J. Bi, X. Jin and R. van der Sman, *J. Food Eng.*, 2023, **351**, 111506.

28 R. Van der Sman, J. Ubbink, M. Dupas-Langlet, M. Kristiawan and I. Siemons, *Food Hydrocolloids*, 2022, **124**, 107306.

29 R. van der Sman, *Food Hydrocolloids*, 2023, 108481.

30 F. Meng, M. Doi and Z. Ouyang, *Phys. Rev. Lett.*, 2014, **113**, 098301.

31 H. Wang and S. Cai, *J. Appl. Phys.*, 2015, **117**, 154901.

32 H. Wang and S. Cai, *Soft Matter*, 2015, **11**, 1058–1061.

33 J. Zhou, X. Man, Y. Jiang and M. Doi, *Adv. Mater.*, 2017, **29**, 1703769.

34 F. Giorgiutti-Dauphiné and L. Pauchard, *Eur. Phys. J. E: Soft Matter Biol. Phys.*, 2018, **41**, 1–15.

35 P. T. A. Nguyen, M. Vandamme and A. Kovalenko, *Soft Matter*, 2020, **16**, 9693–9704.

36 M. Bruning, M. Costalonga, J. Snoeijer and A. Marin, *Phys. Rev. Lett.*, 2019, **123**, 214501.

37 J. Kang, K. Li, H. Tan, C. Wang and S. Cai, *J. Appl. Phys.*, 2017, **122**, 225105.

38 T. D. Wheeler and A. D. Stroock, *Nature*, 2008, **455**, 208–212.

39 J. C. Simo, *Comput. Methods Appl. Mech. Eng.*, 1988, **66**, 199–219.

40 Y. Tang, J. Kang and Y. Q. Wang, *Int. J. Non Linear Mech.*, 2022, **144**, 104076.

41 R. Van der Sman, *Food Hydrocolloids*, 2015, **48**, 94–101.

42 R. Van der Sman, *Soft Matter*, 2015, **11**, 7579–7591.

43 H. Li, *Smart Hydrogel Modelling*, Springer, 2009, pp. 219–293.

44 J. Moya, S. Lorente-Bailo, M. Salvador, A. Ferrer-Mairal, M. Martnez, B. Calvo and J. Grasa, *J. Food Eng.*, 2021, **298**, 110498.

45 A. Drozdov, *Eur. Phys. J. E: Soft Matter Biol. Phys.*, 2014, **37**, 1–13.

46 Z. Ding, W. Toh, J. Hu, Z. Liu and T. Y. Ng, *Mech. Mater.*, 2016, **97**, 212–227.

47 R. Brighenti and M. P. Cosma, *J. Mech. Phys. Solids*, 2022, **169**, 105045.

48 R. Van der Sman, *J. Food Eng.*, 2008, **84**, 400–412.

49 N. Bosnjak, S. Nadimpalli, D. Okumura and S. A. Chester, *J. Mech. Phys. Solids*, 2020, **137**, 103829.

50 R. Van der Sman, *J. Food Eng.*, 2003, **60**, 383–390.

51 R. Van der Sman and M. Meinders, *Food Chem.*, 2013, **138**, 1265–1274.

52 J. Perdana, R. G. van der Sman, M. B. Fox, R. M. Boom and M. A. Schutyser, *J. Food Eng.*, 2014, **122**, 38–47.

53 I. Siemons, R. Boom, R. Van der Sman and M. Schutyser, *Food Hydrocolloids*, 2019, **97**, 105219.

54 M. Tokita and T. Tanaka, *J. Chem. Phys.*, 1991, **95**, 4613–4619.

55 B. Zobrist, V. Soonsin, B. P. Luo, U. K. Krieger, C. Marcolli, T. Peter and T. Koop, *Phys. Chem. Chem. Phys.*, 2011, **13**, 3514–3526.

56 X. He, A. Fowler and M. Toner, *J. Appl. Phys.*, 2006, **100**, 074702.

57 H. Limbach and J. Ubbink, *Soft Matter*, 2008, **4**, 1887–1898.

58 V. Karathanos, A. Kostaropoulos and G. Saravacos, *J. Food Eng.*, 1994, **23**, 481–490.